Section 5

Development of and studies with regional and convective-scale atmospheric models and ensembles.

Improvement of volcanic ash cloud prediction in the Tokyo Volcanic Ash Advisory Center

Kensuke Ishii*[1], Toshiki Shimbori*, Reiko Kai†,
Yoshiomi Hasegawa†, Yosuke Hayashi‡ and Hiroaki Tsuchiyama§

* *Meteorological Research Institute, Tsukuba 305-0052, Japan*
† *Earthquake and Volcanic Engineering Affairs Division, Japan Meteorological Agency, Tokyo 105-8431, Japan*
‡ *Information and Communications Technology Division, Japan Meteorological Agency, Tokyo 105-8431, Japan*
§ *Volcanic Observation Division, Japan Meteorological Agency, Tokyo 105-8431, Japan*

When an explosive eruption occurs, it is vital to predict volcanic ash clouds for aviation safety. The Volcanic Ash Advisory Centers are organizations to predict the ash clouds and issue the Volcanic Ash Advisories (VAAs). One of those is the Tokyo Volcanic Ash Advisory Center (Tokyo VAAC) in the Japan Meteorological Agency (JMA) which has been issuing the VAAs since April 1997.

In the Tokyo VAAC, the VAAs are issued on the basis of predictions from the atmospheric transport model (JMA-ATM; see p5-13 in this report). Generally, ash cloud predictions are governed by ash clouds in initial conditions for ash transport models, because uncertainties of the ash cloud predictions based on the ash transport models inherit uncertainties of the ash clouds in the initial conditions (Folch, 2012). Therefore, it is the key task to improve the initial conditions for the JMA-ATM from ash clouds observations such as those from meteorological satellites.

The satellite analysis by operators in the Tokyo VAAC provides two-dimensional parameters of ash clouds such as areas and top altitudes, whereas vertical profiles including bottom altitudes of ash clouds are not provided. The bottom altitude of an ash cloud is one of the most essential parameters in the initial condition, because an advection direction of the ash cloud depends on the altitude. In an old method of the Tokyo VAAC, some fixed values were used as bottom altitudes of ash clouds in the initial conditions; for example, any ash cloud with top altitude over 10 km always had a bottom altitude of 5 km in spite of a variety of horizontal wind profiles. Therefore, uncertainties of the bottom altitudes of ash clouds caused uncertainties of ash cloud predictions. In order to obtain more accurate bottom altitudes of ash clouds, we developed a new method to estimate the ash clouds thicknesses considering a vertical wind shear from the JMA numerical weather prediction. In this method, an index S which depends on the vertical wind shear is introduced as follows,

$$S = \exp\left[-\alpha C \int_{z_1}^{z_2} \left|\frac{\partial \mathbf{v}}{\partial z}\right| dz\right]$$

where z is the altitude, z_1 and z_2 are the bottom and top altitudes of the ash cloud respectively, $\alpha(= 0.01)$ is constant, $C(= \int_0^{z_{top}} \left|\frac{\partial \mathbf{v}}{\partial z}\right|^{-1} dz)$ is a scaling factor, the vector $\mathbf{v}$

[1]E-mail: kishii@mri-jma.go.jp

is the horizontal wind and $\frac{\partial \mathbf{v}}{\partial z}$ is the vertical wind shear. Then, the bottom altitude z_1 is obtained for $S = 0.3$. The threshold 0.3 was determined from a parameter study. The method provides thinner thicknesses of ash clouds for stronger vertical wind shear, and vice versa.

Fig.1 shows that the introduction of the new method leads to an improvement in the ash cloud prediction. A thickness of the ash cloud in the initial condition is approximately 2 km for the new method, whereas that is approximately 3 km for the old one. Although a validation for the ash clouds thicknesses from the both methods is not sufficient due to a lack of observations, the improvement of ash cloud predictions implies that the new method improves the ash cloud in the initial condition. In fact, ash cloud predictions are improved for many eruption cases not only for the case in Fig.1.

In March 2021, the new method explained above was applied to the ash cloud prediction system in the Tokyo VAAC simultaneously with the update of the JMA-ATM.

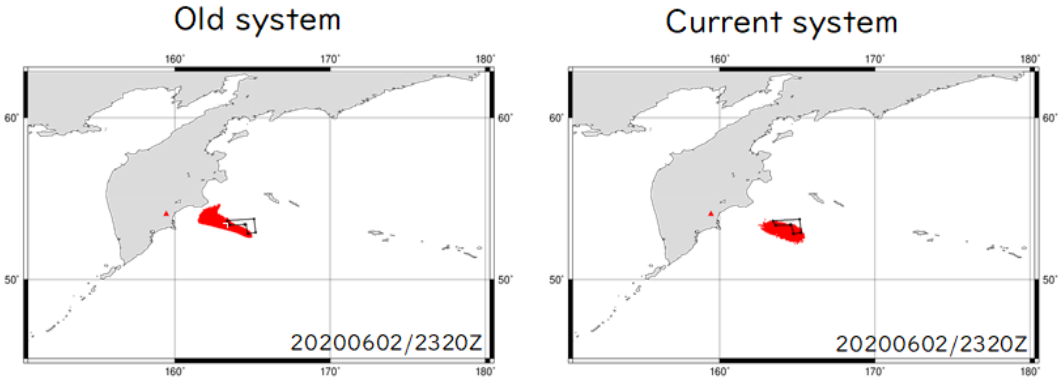

Figure 1: Six-hour ash cloud prediction for the eruption at the Karymsky volcano (▲) on 2 June 2020 (Red dot: ash cloud prediction). The black line shows ash cloud area from satellite analysis.

References

Hasegawa, Y. and Y. Hayashi, 2019: Global atmospheric transport model for volcanic ash. *Outline of the Operational Numerical Weather Prediction at the Japan Meteorological Agency.* JMA, Tokyo, 132-135.

Folch, A., 2012: A review of tephra transport and dispersal models: Evolution, current status, and future perspectives, *J. Volcanol. Geotherm. Res.*, **235-236**, 96-115.

Upgrade of JMA's Mesoscale Ensemble Prediction System

KAKEHATA Takayuki, KUNII Masaru, KAWANO Kohei, and KAWADA Hideyuki
Japan Meteorological Agency
e-mail: t.kakehata@met.kishou.go.jp

1. Introduction

The Japan Meteorological Agency (JMA) began operating the regional ensemble prediction system (Mesoscale Ensemble Prediction System: MEPS; Ono et al. 2021) in June 2019 to provide uncertainty information for its regional Meso-Scale Model (MSM). In September 2020, initial and lateral boundary perturbations in the MEPS were optimized for more appropriate determination of forecast uncertainties around Japan. This report outlines the upgrades and related effects on probabilistic verification scores.

2. Initial Perturbation Upgrade

Mesoscale singular vectors (MSVs) are used for initial perturbations in the MEPS. As detailed in Ono et al. (2021), MSV calculation is based on the simplified version of the JMA non-hydrostatic model (Saito et al. 2006). In the previous system, MSVs tended to be localized over sea areas far south of Japan even when heavy rainfall events were observed around the country (Fig. 1 (a)).

For more efficient clarification of uncertainties related to extreme weather events over the Japan area, adaptive targeting in which a target MSV area is adaptively limited depending on weather conditions was introduced. Here, grid points with 925 hPa vorticity lower than a certain threshold were removed from the predetermined rectangular target area. Figure 1 shows horizontal distributions of total energy (TE) peaks for each MSV with and without adaptive targeting. Here, MSVs corresponding to the uncertainty of rainfall prediction around Japan were successfully calculated as a result of adaptive targeting excluding grid points within the high-pressure system over sea areas south of Japan from the whole target area.

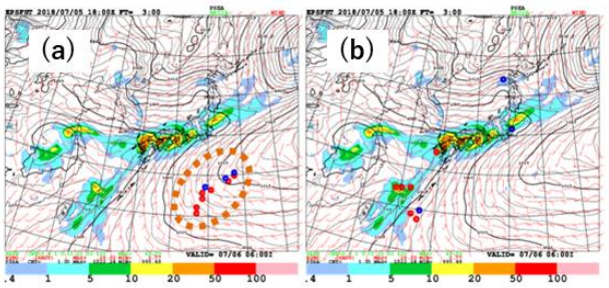

Figure 1. Peak distribution of TE norms for MSV40 (horizontal resolution: 40 km) for the (a) previous and (b) upgraded configurations. The red (blue) points indicate that the corresponding SVs have relatively high (low) growth rates. The initial time is 18 UTC on 5 July 2018.

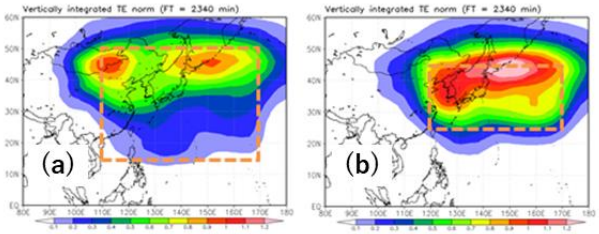

Figure 2. The target area (dashed lines) and normalized total energy distribution at the final time for GSV in the (a) previous and (b) upgraded configurations. Distribution is averaged from 18 June to 21 July 2018.

3. Upgrade of Lateral Boundary Perturbations

3.1 Global SV (GSV) Target Area

Another concern regarding MEPS perturbations was the tendency of the GSVs used as lateral boundary perturbations as well as initial perturbations to focus on uncertainties over desert areas at the northwest edge of the target area (Fig. 2 (a)). GSVs over such areas usually led to poor performance in identifying uncertainties around

Japan, especially with longer lead times. Hence, the GSV target area was reduced to enable focus on the area of interest. This modification contributed to more efficient determination of perturbations over Japan (Fig. 2 (b)).

3.2 Total Energy Norm for GSVs

Following Yamaguchi et al. (2009), the weight of the temperature term in the TE norm adopted in calculating GSVs was changed from 1 to 3 to make perturbations comparable in magnitude to typical analysis errors. This upgrade helps to reduce excessive GSV temperature perturbations and temporary falls in the ensemble spread of temperature at the beginning of simulation.

4. Upgrade Effects

To evaluate the effects of these modifications, experiments with the upgraded configurations (TEST) were compared with the original MEPS (CNTL) over 136 instances in summer 2018 and winter 2017/18. Figure 3 depicts the ensemble spread and the RMSEs of ensemble mean forecasts for 500 hPa geopotential height, with results indicating that the excessive ensemble spread seen in CNTL (particularly in winter) is improved in TEST. Figure 4 illustrates Brier skill scores for three-hour cumulative precipitation forecasts over Japan. Clear improvements in the first half of the forecast range in both summer and winter are seen in TEST, mainly due to the initial perturbation upgrades.

5. Summary

The upgrades to the initial and lateral boundary perturbations introduced into the MEPS in September 2020 enabled more appropriate evaluation of MSM prediction uncertainties around Japan, thereby improving probabilistic precipitation forecasts.

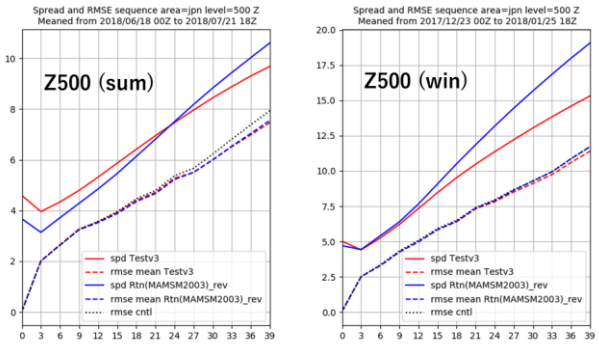

Figure 3. Time-series representations of ensemble spread (lines) and RMSEs of the ensemble mean (dashed lines) for 500 hPa geopotential height in CNTL (blue) and TEST (red).

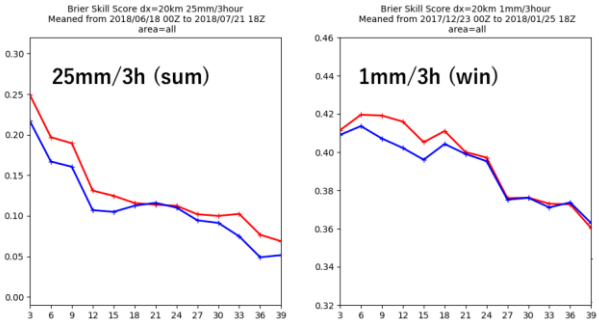

Figure 4. Time-series representations of Brier skill scores for three-hour cumulative precipitation probabilistic forecasts in CNTL (blue) and TEST (red).

Reference

Ono, K., Kunii, M. and Honda, Y., 2021: The regional model-based Mesoscale Ensemble Prediction System, MEPS, at the Japan Meteorological Agency. Quart. J. Roy. Meteor. Soc., 147(734), 465-484.

Saito, K., Fujita, T., Yamada, Y., Ishida, J., Kumagai, Y., Aranami, K., Ohmori, S., Nagasawa, R., Kumagai, S., Muroi, C., Kato, T., Eito, H. and Yamazaki, Y., 2006: The Operational JMA Nonhydrostatic Mesoscale Model. Monthly Weather Review, 134, 1266–1298.

Yamaguchi, M., Sakai, R., Kyoda, M., Komori, T. and Kadowaki, T., 2009: Typhoon Ensemble Prediction System Developed at the Japan Meteorological Agency. Monthly Weather Review, 137, 2592-2604.

Increasing Vertical Resolution and Updating Physical Processes in JMA's Regional NWP System

KUSABIRAKI Hiroshi*, KITAMURA Yuji, SAWADA Masahiro, MATSUBAYASHI Kengo, and NISHIMOTO Shusuke

Numerical Prediction Development Center, Japan Meteorological Agency
*Correspondence to: H. Kusabiraki, Numerical Prediction Development Center, 1-2 Nagamine, Tsukuba, Ibaraki 305-0052, Japan. E-mail: hiro.kusabiraki@met.kishou.go.jp

1 Introduction

A Local Forecast Model (LFM) is used to provide short-range forecasts for disaster mitigation and aviation safety as part of the JMA's operational regional NWP systems (JMA, 2019). This report provides a brief overview of an LFM upgrade from the previous version (LFM2003) to the new version (LFM2103), which went live on 31 March 2021.

2 Increased Vertical Resolution

LFM2003 employed hybrid terrain-following vertical coordinates with the lowest model level height of 20 m. In LFM2103, the number of vertical levels is increased from 58 to 76. The vertical coordinates of the new model have more levels in the Planetary Boundary Layer (PBL) than the old one, with a lowest model level height of 10 m. The increased vertical resolution of LFM2103 allows better representation of surface flux and subgrid turbulent mixing in the PBL.

3 Physics Updates

The various physical parameterisation developments in LFM2103 provide significant improvement in predictive skills over LFM2003 as outlined below.

3.1 Cloud Fraction

LFM2003 was affected by negative bias in Outgoing Longwave Radiation (OLR) in comparison to satellite observation as a result of upper-level cloud fraction overestimation. LFM2103's new cloud fraction scheme based on Wilson and Ballard (1999) reduces ice water content in mixed-phase cloud and ice cloud coverage, thereby reducing OLR biases.

3.2 Turbulent Mixing

The mixed subgrid scale (SGS) vertical transport scheme proposed by Moeng et al. (2010) was introduced in LFM2103. In this scheme, the vertical SGS fluxes are represented by an LFM PBL scheme and a modified Leonard term given by

$$L_{\phi w} = \frac{K_L}{12}\left(\Delta_x^2 \frac{\partial \bar{\phi}}{\partial x}\frac{\partial \bar{w}}{\partial x} + \Delta_y^2 \frac{\partial \bar{\phi}}{\partial y}\frac{\partial \bar{w}}{\partial y}\right), \qquad (1)$$

where Δ_x and Δ_y represent horizontal grid spacing of 2 km, $\bar{\phi}$ represents grid scale variables such as potential temperature and specific humidity, and $\bar{w}$ represents grid scale vertical velocity. K_L is set as 4 based on Verrelle et al. (2017). The Leonard term represents unresolved vertical transport of heat and moisture in deep convection. Figure 1 shows an example of the Leonard term simulated in two-dimensional (2D) idealised deep convection. Upward SGS heat fluxes based on the Leonard term ($L_{\theta w}$, where θ is potential temperature) are represented adjacent to the updraught peak, resulting in reduced grid scale vertical transport.

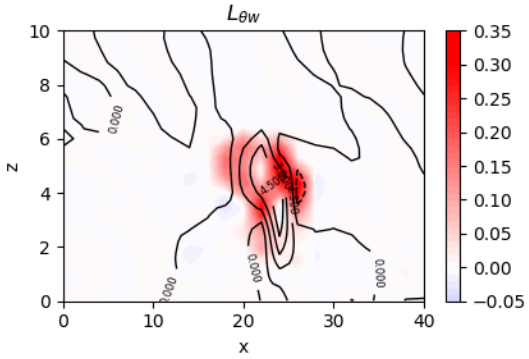

Figure 1: 2D simulation of the Leonard term for potential temperature (K m s^{-1}) given by Eq. (1) based on idealised deep convection with atmospheric profiles initialised in a TRMM-LBA experiment. Black lines denote vertical velocity (m s^{-1}).

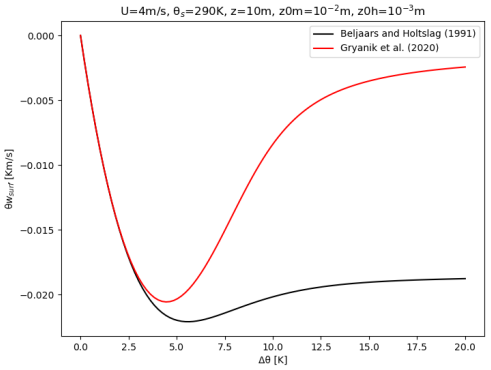

Figure 2: Surface heat flux calculated using the stability functions of Beljaars and Holtslag (1991) (black lines) and Gryanik et al. (2020) (red lines) in a stable boundary layer. The horizontal axis denotes potential temperature differences between the lowest model level and the surface.

3.3 Surface fluxes

In LFM2003, stability functions proposed by Beljaars and Holtslag (1991) (BH91) were used in both stable and unstable boundary layers. For stable

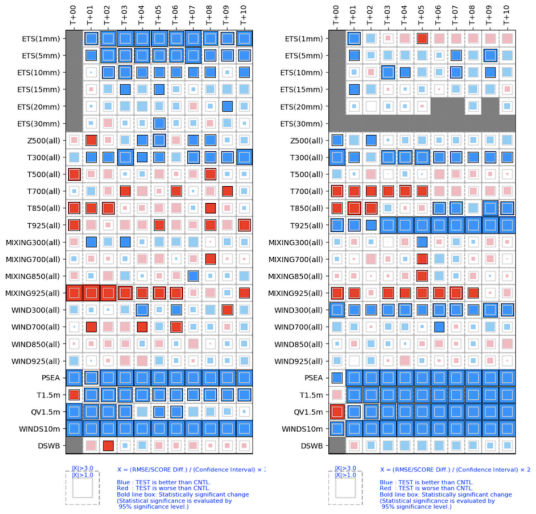

Figure 3: Score difference between LFM2103 and LFM2003 with verification against precipitation based on radar/raingauge precipitation analysis, and synoptic and radiosonde series observation from the experiments conducted in summer (27 June to 8 July 2018; left) and winter (16 January to 27 January 2018; right). Rows represent ETS and RMSE differences for particular parameters, and columns represent forecast ranges from initial to 10 h (T+10). Blue boxes represent increased (reduced) ETS (RMSE) (i.e., improvement), whilst red boxes represent degradation. The area of filled boxes denotes significance, and solid outlines denote statistically significant differences.

boundary layers (SBLs) in LFM2103, the function proposed by Gryanik et al. (2020) (GLGS) was adopted. Figure 2 shows fluxes diagnosed with the stability functions of BH91 and GLGS in an SBL. The GLGS scheme reduces downward heat transport as compared to BH91, thereby mitigating excessive cooling of near-surface air in the SBL.

3.4 Land surface

Ancillary data related to land-surface properties were also significantly changed from the source data used in LFM2103. (i) Thermal roughness lengths over urban surfaces were reduced based on Kanda et al. (2005), and (ii) land surface albedo climatology was updated based on the MODIS Terra and Aqua gap-filled snow-free product. For (ii), most land-surface areas in LFM2103 are darker than those in LFM2003, and (i) and (ii) together achieve a better diurnal cycle for surface temperature. The new model incorporates a subgrid vegetation cover fraction (VCF) supporting accurate latent heat fluxes over non-vegetation surfaces. The maximum green vegetation fraction product developed by Broxton et al. (2014) was applied as the VCF for LFM2103.

4 Evaluation

Figure 3 summarizes the differences in equitable threat scores (ETSs) and root-mean-square errors (RMSEs) between LFM2103 and LFM2003 from NWP forecast skill evaluation. The ETS for rainfall amounts was calculated against radar/raingauge-analysed precipitation, and the RMSE for each field was calculated against synoptic surface and radiosonde observations. Significant improvement in precipitation and near-surface diagnostics is observed, especially for 1.5-m temperature and 10-m wind speed. There are also improvements to temperature at 300 hPa, primarily due to reduced ice cloud fractions. The degradation of lower atmospheric humidity in summer from overestimation of moisture fluxes over the ocean and semi-arid regions in China needs to be tackled in future configurations.

References

Beljaars, A. C. M. and A. A. M. Holtslag, 1991: Flux Parameterization over Land Surfaces for Atmospheric Models. *J. Appl. Meteor. Climat.*, **30**, 327–341.

Broxton, P. D., X. Zeng, W. Scheftic, and P. A. Troch, 2014: A MODIS-Based 1 km Maximum Green Vegetation Fraction Dataset. *J. Appl. Meteor. Climat.*, **53**, 1996–2004.

Gryanik, V. M., C. Lüpkes, A. Grachev, and D. Sidorenko, 2020: New Modified and Extended Stability Functions for the Stable Boundary Layer based on SHEBA and Parametrizations of Bulk Transfer Coefficients for Climate Models. *J. Atmos. Sci.*, **77**, 2687–2716.

JMA, 2019: Outline of the operational numerical wether prediction at the Japan Meteorological Agency. [Available online at `https://www.jma.go.jp/jma/jma-eng/jma-center/nwp/outline2019-nwp/index.htm`].

Kanda, M., T. Kawai, M. Kanega, R. Moriwaki, K. Narita, and A. Hagishima, 2005: A Simple Energy Balance Model for Regular Building Arrays. *Bound.-Layer Meteor.*, **116**, 1573–1472.

Moeng, C.-H., P. P. Sullivan, M. F. Khairoutdinov, and D. A. Randall, 2010: A Mixed Scheme for Subgrid-Scale Fluxes in Cloud-Resolving Models. *J. Atmos. Sci.*, **67**, 3692–3705.

Verrelle, A., D. Ricard, and C. Lac, 2017: Evaluation and Improvement of Turbulence Parameterization inside Deep Convective Clouds at Kilometer-Scale Resolution. *Mon. Wea. Rev.*, **145**, 3947–3967.

Wilson, D. R. and S. P. Ballard, 1999: A microphysically based precipitation scheme for the UK meteorological office unified model. **125**, 1607–1636.

Simulation of polar lows over Norwegian and Barents seas using the COSMO-CLM and ICON models for the 2019–2020 cold season

Anastasia Revokatova [1,2,*], Mikhail Nikitin [1], Gdaliy Rivin [1,3,*], Inna Rozinkina [1,*], Andrei Nikitin [1] and Ekaterina Tatarinovich [1]

[1]Hydrometeorological Research Center of the Russian Federation, Bolshoi Predtechensky per. 11–13, Moscow 123242, Russia;
[2]Yu. A. Izrael Institute of Global Climate and Ecology, Glebovskaya 20B, Moscow 107258, Russia
[3]Geographic Faculty, Department of Meteorology and Climatology, Lomonosov Moscow State University, GSP-1, Leninskie Gory, Moscow 119991, Russia
*Correspondence: revokatova@gmail.com (A.R.); gdaly.rivin@mail.ru (G.R.); inna.rozinkina@mail.ru

Motivations-Introduction

Prediction of polar lows by numerical modelling is a difficult but very crucial task. Polar lows (PLs) are small in size and have a relatively short lifetime, it makes their prediction problematic. Nevertheless PLs, which are rapidly developing, can lead to such extreme weather events as stormy waves, strong winds, the icing of ships, and snowfalls with low visibility, which can influence communication along the Arctic seas. Previous studies using the COSMO model focused on the various factors of polar lows formation, such as sea surface temperature, the presence and position of the ice edge, the strength and presence of a jet stream in one or two PL cases [2,3,4]. In our work, in contrast to previous works, we considered seven polar lows cases which appeared in the Norwegian and Barents Seas last winter. While we did not pay much attention to the factors of PL formation, which are considered in earlier works, we investigated the dependence of the forecast on the lead time and on the model grid steps.

We have identified seven well-developed PLs by the daily analysis of satellite images during the cold period of 2019–2020 (November–March) in the area from Greenland to the Norwegian and Barents seas. The area of investigation with the trajectories of the identified PLs is presented in Figure 1.

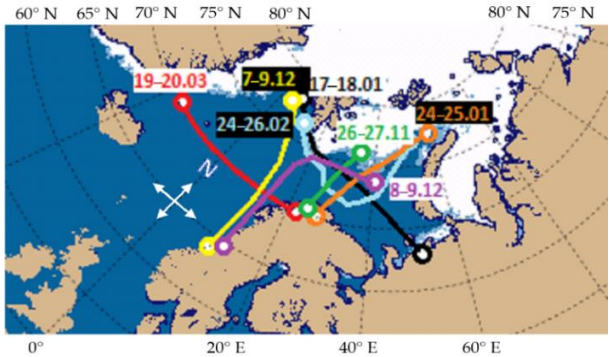

Figure 1. Trajectories of polar lows. Cold period: November 2019–March 2020. The date shows the start point of the trajectory.

2.Models

In this work, we used the COSMO-CLM and ICON Limited-Area models (LAM) [1, 5]. The output of the global ICON model was used for the initial and boundary conditions. The computational domains of all the used model configurations are shown in Figure 2.

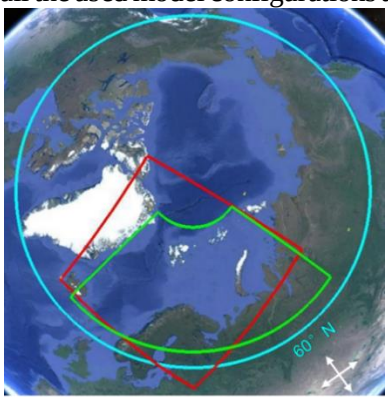

Figure 2. Computational domains. Blue—ICON-A6.5 (with grid spacing 6.5 km); green—ICON-A2 (with grid spacing 2 km); red—COSMO-CLM-A6.6 (with grid spacing 6.6 km).

3.Results

3.1. Comparisons of COSMO-CLM and ICON-A6.5. Case of PL of 20 March 2020

The polar low observed near the Norwegian coast on 20 March 2020, was formed during the day of 19 March in the west of the Norwegian Sea in the cold air flows from the sea ice near the eastern part of Greenland. Then, the vortex moved generally to the east with a steering flow along approximately 70° N, activating during the movement (Figure 3).

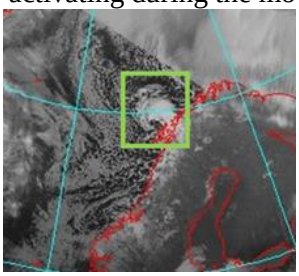

Figure 3. Satellite images of the polar low, 10:00 UTC 20.03. Images available from the Antarctic Meteorological Research Center (AMRC). Polar low shown by square.

The sensitivity of the modelling accuracy to the growth of the forecast lead-time in this case was studied on the basis of numerical experiments with different base times and lead times for the same valid time. With a lead time of 36 h, both models (started 1 day before) produced approximately the same wind gusts, but simulated different locations of the PL (Figure 4 c,d). In 12h forecasts, the PL destruction near the Scandinavian coast was more intense (and additionally quicker for COSMO- CLM) than in reality. With a lead time of 36 h, the PL according to COSMO-CLM was significantly displaced to the northwest (Figure 4c); in the case of ICON, the zone of strong winds was close to that obtained in the experiment with a short lead time (Figure 4a), however the cyclonic vortex itself was reproduced worse (Figure 4d).

3.2. Modelling of PLs with Increasing Model Resolution

The second stage of this work is devoted to an analysis of the forecast quality of the same cases with the ICON model with different resolutions, 2 and 6.5 km, and a study of the structure and peculiarities of the PLs produced by the model, as well as a point data verification using wind speed observations. A noticeable increase in the 10 m wind speed and gusts

was observed at some coastal and island meteorological stations when the PL approached the coast of Norway.

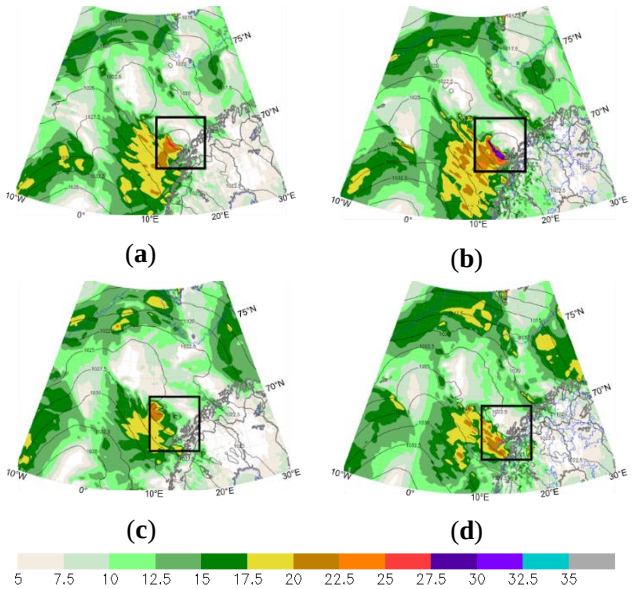

Figure 4. COSMO-CLM-A6.6 (left) and ICON-A6.5 (right) comparison for different lead times: wind gusts and sea-level pressure. Base times: 00:00 UTC 20 March 2020 with a lead time of 12 h (a,b) and 00:00 UTC 19 March 2020 with a lead time of 36 h (c,d). Valid time: 12:00 UTC 20 March 2020. Black square shows the position of the polar low (PL) according to the satellite image.

The simulation results are compared to the coastal observations in Figure 5 (the rectangle shows the time period in which the PLs influenced the coastal wind speed). It can be seen that ICON-A2 and ICON-A6.5 are close in their forecasts. The wind gusts were reproduced accurately; both model configurations also captured the maximum wind speed in the period from 14 to 17 UTC quite successfully. However, the wind weakening in the evening of 20 March was overestimated by the both ICON configurations for Skrova lighthouse.

Conclusions

A number of cases of PL formation in the cold period of 2019/2020 were identified over the Barents and Norwegian seas using satellite images. Numerical experiments using the COSMO-CLM and ICON models with a grid spacing of about 6.6 km and 6.5 km were carried out in the first part of this work. All the cases of detected PL were successfully simulated by all configurations. However, a rapid decrease in the accuracy of the modelling results was detected after the first 24 h of the forecast for all configurations. We can suppose that our simulations could benefit from taking into account temporal variations of the sea surface during the forecast as well as from data assimilation. Note also that the initial data in our experiments were taken from the global model with 13 km grid spacing. The difference between the ICON and COSMO simulations with the same resolution was bigger than that between simulations with two configurations of ICON. Some results showed that ICON-A2 was a little more accurate than ICON-A6.5, but the advantages of ICON-A2 are not always obvious. Simulations with ICON-A2 provide more detailed maps of wind speed, wind gust, and vorticity in comparison with ICON-A6.5 simulations.

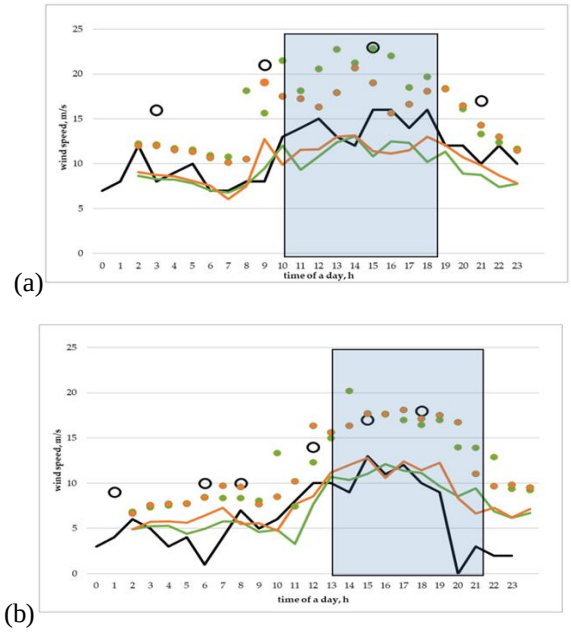

Figure 5. ICON-A6.5 (orange); ICON-A2 (green); observations (black): 10 m wind speed (curves) and wind gusts (circles) on 20 March 2020. (a) Airport Röst (67°31’ N, 12°06’ E); (b) Skrova lighthouse (68°09’ N, 14°39’ E)

But point-to-point verification did not show significant advantages of ICON-A2. Orographic features of the surface can strongly influence the wind speed forecast in the polar low when it comes to the land. Detailed research of the polar lows over Norwegian and Barents Seas using the COSMO-CLM and ICON models for the 2019–2020 Cold Season can be found in [6]

Funding: This research is funded by the Federal Service for Hydrometeorology and Environmental Monitoring of Russia (topics AAAA-A20-120021490060-1(mainly) and AAAA-A20-120021890120-8 (predictability analysis))

References:

1) Baldauf, M., A. Seifert, J. Förstner, D. Majewski, M. Raschendorfer, and T. Reinhardt. Operational convective-scale numerical weather prediction with the COSMO model: Description and sensitivities. Mon. Wea. Rev. 2011, 139(12), p. 3887-3905

2) Nikitin, M.A.; Rivin, G.S.; Rozinkina, I.A.; Chumakov, M.M. Identification of polar cyclones above the Kara Sea waters using hydrodynamic modelling. *Vesti Gazov. Nauki* 2015, *22*, 106–112. (In Russian)

3) Nikitin, M.A.; Rivin, G.S.; Rozinkina, I.A.; Chumakov, M.M. Use of COSMO-Ru forecasting system for polar low's research: Case study 25–27 March 2014. *Proc. Hydrometcentre Russ*. 2016, *361*, 128–145. (In Russian)

4) Rivin, G.; Nikitin, M.; Chumakov, M.; Blinov, D.; Rozinkina, I. Numerical Weather Prediction for Arctic Region. *Geophys. Res. Abstr*. 2018, *20*, EGU2018–EGU5505.

5) Zängl, G., D. Reinert, P. Rípodas, and M. Baldauf. The ICON (ICOsahedral Non-hydrostatic) modelling framework of DWD and MPI-M: Description of the non-hydrostatic dynamical core. Q. J. Roy. Meteor. Soc. 2015, 141(687):563-579.

6) Revokatova, A.; Nikitin, M.; Rivin, G.; Rozinkina, I.; Nikitin, A.; Tatarinovich, E. High-Resolution Simulation of Polar Lows over Norwegian and Barents Seas Using the COSMO-CLM and ICON Models for the 2019–2020 Cold Season. Atmosphere 2021, MDPI, V 12, № 1, 137. https://doi.org/atmos12020137

COSMO-Ru System: Status and Scientific Projects Including Testing of ICON-NWP

Gdaliy Rivin [1,2,*], Inna Rozinkina[1,2], Elena Astakhova[1], Denis Blinov[1], Anastasia Bundel'[1], Nataliya Chubarova[1,2], Irina Gorlach[1], Alexander Kirsanov[1], Marina Shatunova[1], Dmitriy Alferov[1], Mikhail Varentsov[1,2], Timofeiy Samsonov[1,2], Denis Zakharchenko[1], Philipp Bykov[1], Julia Khlestova[1,2], Vladimir Kopeykin[1], Mikhail Nikitin[1], Alexey Poliukhov[1,2], Anastasia Revokatova[1,3], Ekaterina Tatarinovich[1].

[1] *Hydrometeorological Research Center of the Russian Federation, Bolshoi Predtechensky per. 11–13, Moscow 123242, Russia;* [2] *Lomonosov Moscow State University, Moscow, Russia;* [3] *Yu. A. Izrael Institute of Global Climate and Ecology, Glebovskaya 20B, Moscow 107258, Russia.*

* Correspondence: gdaly.rivin@mail.ru

Status of COSMO-Ru System

The **operational short-range numerical weather prediction (NWP) system COSMO-Ru** of the Hydrometeorological center of Russia currently uses various configurations of COSMO v. 5.8 model of the meteorological European consortium of the same name as an atmospheric model and SGI ICE-X (peak performance 14 Tflops), T-Platforms V6000 (800 Tflops) and Cray XC40-LC (1.3 Pflops) as computers (http://www.mcc.meteorf.ru/oborudovanie.html).

Figure 1 presents the COSMO-Ru system on SGI ICE-X as at the beginning of 2020. Integration domains for different configurations are shown in color. The list of configurations (their name, the number of grid points, the grid spacing) is given at the top of the plot in colors corresponding to those in the map. For the configuration COSMO-RuENA with the largest integration domain 120-h forecasts were issued.

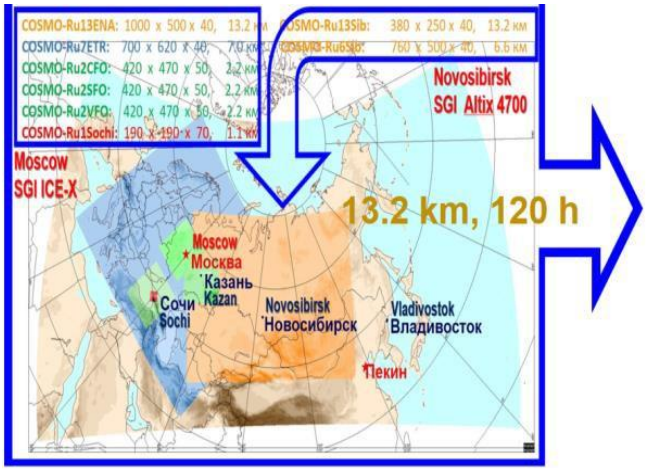

Fig. 1. System COSMO-Ru as at the beginning of 2020 on the SGI ICE-X cluster.

Note that for the Urals and Siberia region, highlighted brown in the plot, weather forecasts were issued also using the COSMO-Ru system with a grid spacing of 13.2 km but at the Novosibirsk WMO regional center. For this, a slightly modified configuration was prepared jointly with Novosibirsk colleagues.

At present, the COSMO-Ru system has been transferred to the Cray computer, with a decrease in the grid spacing for ENA (from 13.2 km to 6.6 km) and an extension of the integration area with a grid spacing of 2.2 km.

The relevant information about configurations of the COSMO model (domains, the corresponding grids, the forecast lengths) is shown in Figure 2. With the advent of the T-Platforms V6000 computer at the Main Computing Center of Roshydromet, the work has begun on implementing the COSMO-Ru system on it as a backup of its versions on SGI ICE-X and Cray XC40-LC "Roshydromet". This will guarantee sustainable issuance of numerical weather forecasts using the COSMO-Ru system.

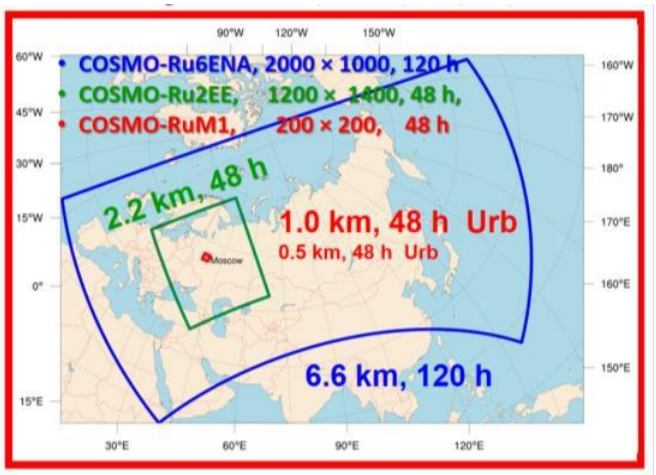

Fig. 2. System COSMO-Ru with COSMO model configurations on the Cray XC40-LC "Roshydromet".

The operational short-range NWP system COSMO-Ru runs 4 times a day and prepares more than 8000 maps, 1200 meteograms and T-skew diagrams. Additionally, 2 times per day a configuration COSMO-Ru2ART runs for the pollution forecast with a grid spacing of 2.2 km for Moscow region.

Testing of ICON-NWP

Currently, the COSMO consortium is working to replace the non-hydrostatic COSMO model for a limited area with a new ICON model [*Zängl et al, 2015*], which has greater capabilities and better forecasting skill.

In this regard, the Hydrometcenter of Russia is working on replacing the COSMO model configurations in the COSMO-Ru system with the ICON model configurations for short-term forecasting not only for a limited area, but also for the entire Earth (90 levels up to 75 km).

Figure 3 shows the domains of integration including the nested ones and the results of numerical experiments with different numbers of cores made for choosing optimal configurations. A 5-day forecast by the global ICON model with nesting (a grid step of 6.5 km to the north of 30^0N and 13 km for the rest of the region, 90 vertical levels up to 75 km) requires 42 min of processor time using 5760 cores for computations and 32 cores to organize the input / output process.

Fig. 3. System COSMO-Ru with configurations ICON-Ru (global and regional (LAM)) on the Cray XC40-LC "Roshydromet".

Scientific Projects

To develop and improve the COSMO and ICON models, research is carried out within the framework of projects of Roshydromet and the COSMO consortium, considering various atmospheric processes and components (aerosol [*Poliukhov, Blinov, 2021*], clouds and radiation [*Khlestova et al, 2020; Shatunova et al, 2020*], ensembles [*Astakhova et al, 2020*], the fires in Siberian forests [*Kirsanov et al, 2020*], polar lows [*Revokatova et al, 2021*], tornadoes [*Chernokulsky et al, 2020*], urban [*Galbero et al, 2020; Rivin et al, 2020; Varentsov et al, 2020*]), using machine learning methods in post-processing [*Bykov, 2020*], verification, etc.

References

Astakhova E., Alferov D., Alferov Y., Bundel A. Ensemble approach to weather forecasting // Journal of Physics: Conference Series (JPCS), vol 1740, CSP 2020, 012070, 10 pp. DOI: 10.1088/1742-6596/1740/1/012070

Bykov F.L. Statistical Correction of the COSMO Model Weather Forecasts Based on Neural Networks // Russ. Meteorol. Hydrol, 2020. Vol. 45. P. 141–152. DOI: 10.3103/S1068373920030012.

Chernokulsky A., Kurgansky M., Mokhov I., Shikhov A., Azhigov I., Selezneva E., Zakharchenko D., Antonescu B., Kuhne T. Tornadoes in Northern Eurasia: from the Middle Age to the Information Era // Mon. Wea. Rev., 2020. V.148, N 8, p. 3081-3110. https://doi.org/10.1175/MWR-D-19-0251.1

Garbero V., Milelli M., Bucchignani E., Mercogliano P., Varentsov M., Rivin G., Blinov D., Wouters H., Shultz J.-P., Shattler U., Bassani F., Demusere M., Repola F. F. Evaluating the Urban Canopy Scheme TERRA_URB in the COSMO Model for Selected European Cities // Atmosphere, 2021, 12 (2), 237. https://doi.org/10.3390/atmos12020237

Khlestova J., Chubarova N., Shatunova M., Rivin G., Becker R., Görsdorf U., Mayer B., Pospichal B., Seifert P., Zinner T. Radiative and temperature effects of experimental cloud-radiation interaction scheme of COSMO model // 26th International Symposium on Atmospheric and Ocean Optics: Atmospheric Physics. 2020. Vol.11560, 115600C. DOI: 10.1117/12.2575575.

Kirsanov A., Rozinkina I., Rivin G., Zakharchenko D., Olchev A. Effect of Natural Forest Fires on Regional Weather Conditions in Siberia // Atmosphere, 2020. Vol. 11, no. 10. 1133. DOI: 10.3390/amos11101133. ISSN: 2073-4433

Poliukhov A., Blinov D. Aerosol Effects on Temperature Forecast in the COSMO-Ru // Russian Meteorology and Hydrology, 2021. V. 46, no. 1. P. 19-27. https://doi.org/10.3103/S1068373921010039

Revokatova A., Nikitin M., Rivin G., Rozinkina I., Nikitin A., Tatarinovich E. High-Resolution Simulation of Polar Lows over Norwegian and Barents Seas Using the COSMO-CLM and ICON Models for the 2019-2020 Cold Season // Atmosphere, 2021, 12 (1), 137. https://doi.org/atmos12020137

Rivin G.S., Rozinkina I.A., Vil'fand R.M., Kiktev D.B., Tudrii K.O., Blinov D.V., Varentsov M.I., Zakharchenko D.I., Samsonov T.E., Repina I.A., Artamonov A.Yu. Development of the High-resolution Operational System for Numerical Prediction of Weather and Severe Weather Events for the Moscow Region // Russian Meteorology and Hydrology, 2020. Vol. 45, no. 7. P. 455-465. DOI: 10.3103/s1068373920070018.

Shatunova M.V., Khlestova Y.O., Chubarova N.E. Forecast of microphysical and optical characteristics of large-scale cloud cover and its radiative effect using the COSMO mesoscale weather prediction model // Atmospheric and Oceanic Optics. 2020. Vol. 33, no. 2. P. 154-160. DOI: 10.1134/S1024856020020098.

Varentsov M., Samsonov T., Demuzere M. Impact of Urban Canopy Parameters on a Megacity's Modelled Thermal Environment// Atmosphere, 2020,11(12),1349. https://doi.org/10.3390/atmos11121349

Zängl G., Reinert D., Rípodas P., Baldauf M. The ICON (ICOsahedral Non-hydrostatic) modelling framework of DWD and MPI-M: Description of the non-hydrostatic dynamical core // Q. J. R. Meteorol.Soc. 2015. V. 141. № 687. P. 563–579. https://doi.org/10.1002/qj.2378

Renewal of the JMA Atmospheric Transport Model on the Volcanic Ash Advisory and Ash Fall Forecast Distribution System

Toshiki Shimbori[*], Kensuke Ishii[*], Reiko Kai[†],
Yoshiomi Hasegawa[†], Yosuke Hayashi[‡] and Yuta Hayashi[§]

[*]*Meteorological Research Institute, Tsukuba 305-0052, Japan*

[†]*Earthquake and Volcanic Engineering Affairs Division, Japan Meteorological Agency, Tokyo 105-8431, Japan*

[‡]*Information and Communications Technology Division, Japan Meteorological Agency, Tokyo 105-8431, Japan*

[§]*Volcanic Observation Division, Japan Meteorological Agency, Tokyo 105-8431, Japan*

The Japan Meteorological Agency (JMA) has been issuing volcanic ash advisories (VAAs) since April 1997 and volcanic ash fall forecasts (VAFFs) since March 2008. VAAs had been mainly based on the outputs of global atmospheric transport model (JMA-GATM; Hasegawa and Hayashi, 2019a) since December 2013, while VAFFs had been based on the other outputs of regional atmospheric transport model (JMA-RATM; Shimbori et al., 2009; Hasegawa and Hayashi, 2019b) since the beginning. The JMA-GATM was driven by the gridded data of the global spectral model (GSM) and the JMA-RATM by those of the meso-scale model (MSM) or local forecast model (LFM) based on the nonhydrostatic model ASUCA.

In March 2021, we have developed the new atmospheric transport model (JMA-ATM; Shimbori and Ishii, 2021) to unify the JMA-GATM and JMA-RATM, and then implemented in the JMA's supercomputer system connected to the volcanic ash advisory and ash fall forecast distribution system (VAFS). Main features of the JMA-ATM are as follows: This model is an offline Lagrangian model, which the time tendency of tracer variables is calculated in each process and integrated at the last time step in order that dynamical and physical processes are commutative at each time step. The element conversion of gridded data is executed during preprocessing. The coordinate system of the JMA-ATM can accommodate beyond the input datasets of the GSM, MSM and LFM, i.e. the vertical coordinates of the JMA-GATM and JMA-RATM are the σ-p hybrid coordinate of the GSM and the hybrid terrain-following coordinate of the ASUCA, respectively, but the JMA-ATM unifies the models by converting the gridded data to identical z-coordinates. Hence previous workflows on the supercomputer had two independent main flows corresponding to the JMA-GATM and JMA-RATM; on the other hand, current workflows consist of several preprocessors and one main flow corresponding to the JMA-ATM (Fig. 1).

An example of volcanic ash fall predictions is shown in Fig. 2. As an operational model, a first objective of the JMA-ATM, which is to maintain the accuracy of JMA-GATM and JMA-RATM predictions, has been achieved.

[*] E-mail: shimbori@met.kishou.go.jp

References

Hasegawa, Y. and Y. Hayashi, 2019a: Global atmospheric transport model for volcanic ash. *Outline of the Operational Numerical Weather Prediction at the Japan Meteorological Agency*. JMA, Tokyo, 132–135.

Hasegawa, Y. and Y. Hayashi, 2019b: Regional atmospheric transport model for volcanic ash. *Outline of the Operational Numerical Weather Prediction at the Japan Meteorological Agency*. JMA, Tokyo, 135–138.

Shimbori, T., Y. Aikawa and N. Seino, 2009: Operational implementation of the tephra fall forecast with the JMA mesoscale tracer transport model. *CAS/JSC WGNE Res. Activ. Atmos. Oceanic Modell.*, **39**, 0529–0530.

Shimbori, T. and K. Ishii, 2021: Design of the Japan Meteorological Agency atmospheric transport model. *Tech. Rep. MRI*, **84**, 146 pp.

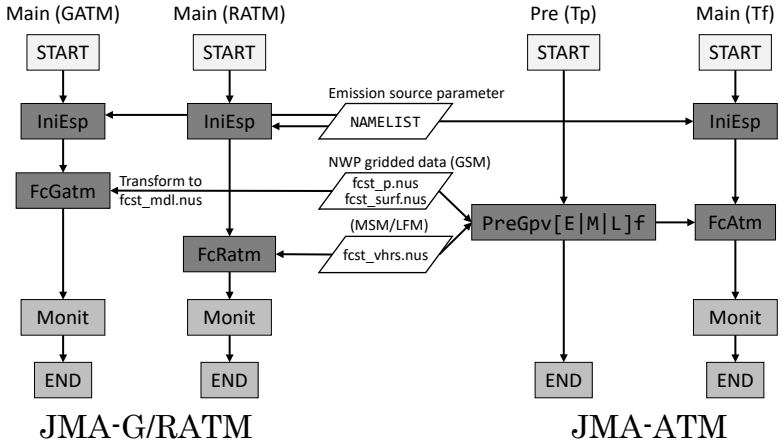

Fig. 1 Comparison of workflows (see Fig. B.1 of Shimbori and Ishii (2021))

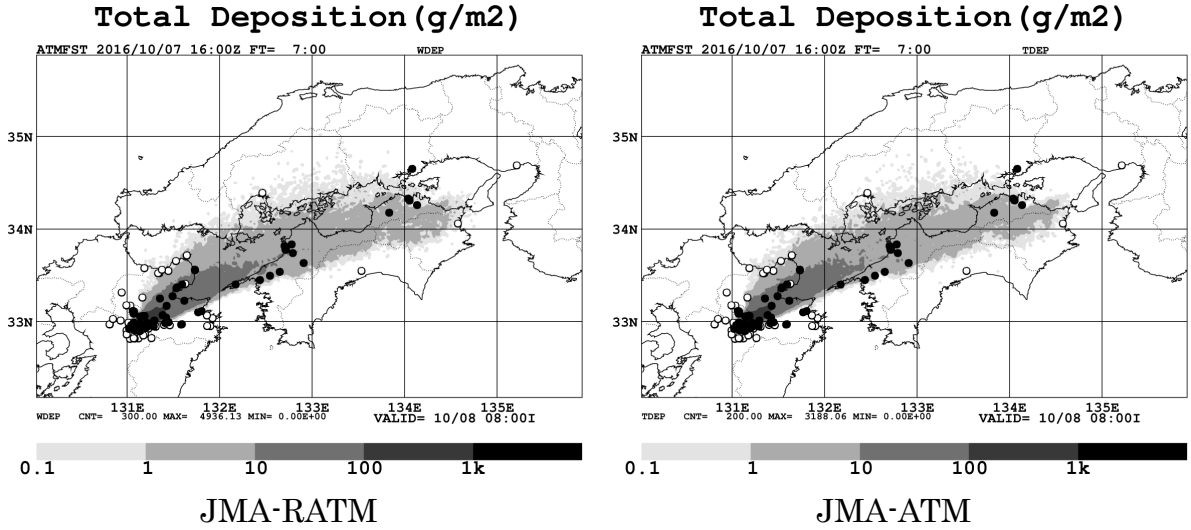

Fig.2 Six-hour volcanic ash fall predictions of the eruption at Aso Volcano on 7 Oct. 2016 from the event time at 16:46 UTC to the valid time at 23:00 UTC with a plume height of 11,800 m above the crater. The symbols of ash-fall observations are as follows: ● observed; ○ unobserved. (see Fig. 5.13 of Shimbori and Ishii (2021))